Energy Conversion and Management 302 (2024) 118145

Contents lists available at ScienceDirect

Energy Conversion and Management

journal homepage: www.elsevier.com/locate/enconman

Research Paper

Optimisation of $CaCl_2$ impregnated expanded graphite and alginate matrices – Targeted salt loading

Jack Reynolds [a,*], Bahaa Abbas [a], Geraint Sullivan [a], Jonathon Elvins [a], Eifion Jewell [a], Justin Searle [a], Lorena Skevi [b], Xinyuan Ke [b]

[a] Specific IKC, Baglan Bay Innovation Centre, Swansea University, Central Avenue, Port Talbot SA12 7AX, UK
[b] Department of Architecture and Civil Engineering, University of Bath, Claverton Down, Bath BA2 7AY, UK

ARTICLE INFO

Keywords:
Thermal energy storage
Expanded graphite
Calcium chloride
Alginate
Salt loading

ABSTRACT

The incorporation of salt hydrates in thermochemical energy storage is often limited by poor kinetics and mechanical instability during charge and discharge cycles. This study explores the influence of salt loading on the energy storage capacity and charge/discharge performance of salt-impregnated expanded graphite and alginate composites. By controlling the salt bath concentration during composite synthesis, the quantity of salt within the bead can be regulated. Four composites have been synthesised with salt wt% values ranging from 63.7 to 77.2 %, resulting in salt volumetric densities form 0.22–0.52 g/cm^3 and energy densities between 1052 and 1281 kJ/kg. The study found that increasing salt bath concentration above 60 % significantly decreases the porosity within the composite. This reduces moisture transfer kinetics and also fails to accommodate for salt expansion and deliquescence. Consequently, composites at near-maximum salt capacity displayed diminished discharge performance and charge efficiency. Conversely, samples below the saturation threshold exhibited greater heat output and charge efficiency, contained overhydration, and maintained structural integrity. These findings highlight the importance of carefully balancing energy storage capacity with improved reaction kinetics and stability to achieve an optimal storage solution in solar thermal systems or waste heat recovery.

1. Introduction

Energy consumption and the demand for clean energy sources have become increasingly important due to global climate changes. Fossil fuels still account for almost 50 % of the energy used for building-related heating in the UK, and with the ever-increasing costs associated with these fuels, a shift towards renewable energy sources is urgently needed [1,2]. Alternative sources of heat can include heat direct from renewables (wind or solar), heat pumps powered via solar, or the re-utilisation of industrial waste heat [3–7]. Yet, the availability of these energy sources can be geographically or seasonally dependent, leading to a mismatch between when energy is produced and when it is needed.

To address these challenges, robust long-duration thermal storage solutions are essential, with the added flexibility of transportability between sites. While traditional thermal energy storage methods like sensible heat storage are known for their lower cost, they are often limited by low energy densities and short storage durations. Similarly, latent heat storage, despite being a more modern approach due to higher associated energy density, also shares the limited storage duration characteristic [8]. Alternatively, heat can be stored thermochemically, where the energy is stored in the breaking and forming of chemical bonds [9]. This method offers a higher energy density and the capacity for long-term heat storage, but research into this technique is still in the pilot stages.

Sorption thermal energy storage (STES), specifically salt hydrates, represent a promising category of materials for long-term thermochemical energy storage [10,11]. The anhydrous salt expels heat upon reaction with water (hydration) to form crystalline hydrates, and they store energy when supplied with excess heat (dehydration) to revert to their anhydrous form. This reversible process can be represented by Equation (1):

$$Salt + xH_2O \rightleftharpoons Salt.xH_2O + HEAT \quad (1)$$

A successful application of salt hydrates in a packed bed heat battery

* Corresponding author.
E-mail addresses: 865797@swansea.ac.uk (J. Reynolds), B.H.A.Abbas@Swansea.ac.uk (B. Abbas), G.L.Sullivan@Swansea.ac.uk (G. Sullivan), Jonathon.Elvins@Swansea.ac.uk (J. Elvins), E.Jewell@Swansea.ac.uk (E. Jewell), J.R.Searle@Swansea.ac.uk (J. Searle), ls2154@bath.ac.uk (L. Skevi), xk221@bath.ac.uk (X. Ke).

https://doi.org/10.1016/j.enconman.2024.118145
Received 27 November 2023; Received in revised form 9 January 2024; Accepted 24 January 2024
Available online 7 February 2024

faces significant challenges, including insufficient kinetics during gaseous reactions and agglomeration resulting from overhydration [12]. Stability could in principle be guaranteed when overhydration can be prevented by controlling the humidity below the deliquescence relative humidity (DRH), however output power will be compromised due to further reductions in kinetics.

Aristov et al. suggested novel composites called "salt in porous matrix", which solve the problems of swelling and agglomeration while increasing total sorption capacity and energy storage density [13]. In these materials, the matrix, traditionally employed for sorption heat storage, now serves exclusively as a host to prevent the deliquescence of the salt during hydration. Examples of such matrices include molecular sieves [14,15], Carbon based structures [16,17], and silica Gel [18].

Selecting an appropriate porous matrix for STES systems requires careful consideration of multiple factors, including stability, porosity, volumetric energy storage density, and efficient heat/mass transfer. One of the most common choices for a matrix is expanded vermiculite [19–23]. It is a simple and inexpensive matrix that can be filled using the incipient wetness technique to well controlled targets [24], making it easily compatible with most salt hydrates. However, the vermiculite-based composites have an associated low bulk density (0.2 g/cm^3), corresponding to a low salt volumetric density, and also a low thermal conductivity (0.05 W/mK) [25]. Alternatively expanded graphite is known for its large surface area and excellent thermal transport properties, capable of enhancing the thermal conductivity of the STES composites by fivefold [26]. However, additional efforts are required to ensure the stability of the structures. This has been accomplished through the use of organic binders and techniques like pelletisation and freeze-drying [27,28].

The development of a millimeter-scale polymeric matrix (crosslinked pHEMA) has demonstrated promising results in stabilising salt hydrates (K_2CO_3, $CaCl_2$, and LiCl) within its highly porous structure [29]. It effectively contains deliquescence and achieves a higher power output than the pure salt hydrate equivalent, although the energy density is significantly lower in comparison. An alternative cross-linked polymer with high salt loading capabilities is an alginate-based hydrogel [30–32]. This has been considered as a host matrix due to its exceptional microscopic shaping capabilities through either a drop-cast or frozen mould method. The size and shaping ability aids system design by preventing large pressure drops across the reactor bed, a common issue when using raw salt hydrates [33]. The matrix is formed through a cross-linking reaction with a divalent cation (2+ cation), allowing salts like $CaCl_2$ and $SrCl_2$ to serve as both the cross-linking agent and the active salt that fills the hydrogel's pores. Additionally, $MgSO_4$ and $MgCl_2$ have been incorporated as active salts. These were initially incorporated as a precursor material ($Mg_5(CO_3)_4(OH)_2{\cdot}4H_2O$) and later chemically modified. The gelation salt, in this case, was calcium lactate.

The authors of this paper conducted a comprehensive investigation into the development and characterisation of three novel composites that combine expanded graphite with an alginate polymer [32]. The alginate polymer facilitates matrix shaping through gelation, while the expanded graphite provides a highly porous structure with a high surface area and thermal conductivity, making it suitable for retaining thermochemically active salts. The researchers also compared these composites with a traditional SIM material that uses vermiculite as a host matrix. Among the three materials studied, the mEG-M composite emerged as the most promising. This composite utilised a milled form of expanded graphite (mEG) combined with alginic acid (Alg) and employed the mould method (M) combined with an ice-templating technique prior to gelation.

This work introduces an approach to regulate the salt loading of the mEG-M composite, enabling an investigation into the correlation between salt loading and porosity and how it impacts the performance of charge and discharge cycles. The optimisation methodology offers a new perspective by exploring how fine-tuning salt loading can lead to significant improvements in the achievable energy storage capacity (as appose to the theoretical value), which is dependent on both hydration and dehydration efficiency, and also the stability of the composites. This approach highlights that maximising salt loading within a matrix does not fully address the challenges associated with pure salt hydrates. Instead, it demonstrates that controlling salt levels is crucial in influencing key parameters essential for a successful thermochemical heat storage solution.

2. Materials and methods

2.1. Materials

Anhydrous calcium chloride was purchased from Sigma-Aldrich® and the solutions of specific saturation were prepared at room temperature. Alginic acid, sodium salt was purchased from Fischer Scientific in powder form. Milled expanded graphite, commercial grade TIMREX® C-THERM012, with 25 m^2/g surface area (as reported in the material data sheet) was purchased from Imerys Graphite & Carbon (Bironico, Switzerland).

2.2. Composite synthesis

Fig. 1 highlights the synthesis procedure of salt incorporated expanded graphite & alginate composites utilising the mould method for gelation. The mould is custom-fabricated in-house using a 3D-printed template and mould making Polycraft GP3481-F silicone rubber. The bead diameter within the mould is set at 7 mm. During the Mould method the pre-cast mixture is frozen and dropped in a $CaCl_2$ bath. The salt content of the beads can then be regulated by controlling the $CaCl_2$ concentration within the bath. To regulate the salt bath concentration, the water quantity in the pre-cast mixture must be estimated first.

A standard sodium alginate solution (1 g/50 ml) with a known mEG: Alg ratio (6:1) is used, and the amount of water added to the water bath can be calculated based on the amount of pre-cast mixture used. For this study, four composites were prepared with different concentrations (mEG100, mEG80, mEG60, and mEG40), where the number indicates the water bath concentration. The estimated proportions of each material in the pre-cast mixture are highlighted in Table 1, allowing for the calculation of the total water incorporated in the salt bath and the required amount of salt to achieve each concentration level. The bath concentration is determined using the theoretical maximum solubility of $CaCl_2$ at standard conditions (74.5 g/100 ml), which equates to a mass ratio of $CaCl_2$ of 0.745 to that of water (for every 1 g of water, there are 0.745 g of $CaCl_2$) or a 100 % saturation [20]. The subsequent saturation values are then calculated as a percentage of this value.

2.3. Experimental procedures

2.3.1. Physical characterisation

In order to analyse the internal structure of the composite beads, a Hitachi TM4000Plus II desktop scanning electron microscope (SEM) operating at a 15 kV accelerating voltage was employed. Additionally, electron dispersive spectroscopy (EDS) was utilised to evaluate the distribution and coverage of salt within the internal structure of the beads. The beads were sliced to create semi-spherical structures with a flat plane passing through the centre.

The bulk density of the sample was calculated from their mass reading (measured on an Ohaus Scout STX223 with a readability of 0.001 g) in a known volume of a cylindrical container. The volume of the container is calculated from the filled mass of water (1 g = 1 cm^3).

The salt loading of the composites was determined using a titration analysis of chloride ion concentration, employing Mohr's Method. To dissolve all the $CaCl_2$ present, the composite (3 g) was washed in 100 ml of deionised (DI) water for >1 h. A silver nitrate solution was used, along with a potassium chromate indicator, to titrate this solution. The $AgNO_3$ solution reacted preferentially with chloride ions, resulting in the

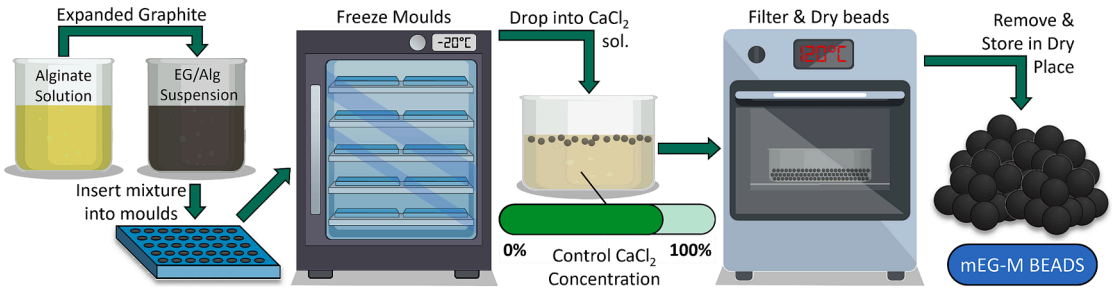

Fig. 1. Schematic illustration of fabrication of $CaCl_2$ impregnated mEG/Alg beads using the mould method.

Table 1
Material formulation.

Sample	Saturation [%]	$CaCl_2$ Mass Ratio	Mass of Material [g]	mEG [g]	Alg [g]	Water [g]	Water Bath [g]	Total Water [g]	$CaCl_2$ [g]
mEG100	100 %	0.745	250	26.3	4.4	219.3	500	719	535.9
mEG80	80 %	0.596	250	26.3	4.4	219.3	500	719	428.7
mEG60	60 %	0.447	250	26.3	4.4	219.3	500	719	321.5
mEG40	40 %	0.298	250	26.3	4.4	219.3	500	719	214.4

formation of a precipitate of AgCl. The colour change from yellow to orange indicated the formation of silver chromate, indicating the complete consumption of chloride ions. The chloride ion concentration was determined from the titration volume, enabling the calculation of the $CaCl_2$ present in the sample.

The size distribution of the composites was examined using a Keyence VHX-7000 digital microscope. The bead diameter in the x and y planes was calculated for 20 beads from each sample, and an average value was determined.

Mercury intrusion porosimetry (MIP) of the four samples was conducted using a Micromeritics AutoPore V 9600 analyser. Each run consisted of a penetrometer volume of 6.7650 ml, containing six beads. The samples were prepared by drying at 120 °C for 24 h which were then allowed to cool to room temperature within a sealed container. For each sample run, the pressure was incrementally increased from 0.85 psia to a maximum pressure (P_{max}) of 60,000 psia. Subsequently, the pressure gradually decreased back to 28 psia.

2.3.2. Thermal characterisation

The thermophysical properties of the synthesised composites were measured using a hot disk thermal constant analyser (TPS-1000, Hot Disk Inc., Sweden). Bulk samples were placed within a cylindrical container with an inner diameter of 60 mm and a height of 80 mm. A 4922 sensor with a radius of 14.6 mm was positioned at the centre of the cylinder, ensuring equal amounts of material (40 mm) above and below the sensor. Prior to measurement, the samples were dried at 120 °C for 24 h to achieve an anhydrous state. The thermal conductivity (k) and specific heat (cp) of the bulk samples were measured five times for three filled containers of each material. This approach allowed for an average to be calculated, accounting for discrepancies resulting from variations in the packing of the beads during each measurement.

The dehydration enthalpy was evaluated using differential scanning calorimetry (DSC) conducted in the DSC Q20 (TA Instruments) in combination with thermogravimetric analysis (TGA) performed in a Pyris 1 (Perkin Elmer). Prior to both tests, materials were placed in the Memmert constant climate chamber (HPP110eco) under controlled temperature and humidity of 25 °C and 25 % RH until no further mass loss was observed. This was done to achieve the maximum hydrated state for $CaCl_2$ (hexahydrate) while preventing over hydration leading to deliquescence. Subsequently, the hydrated beads were crushed into powder with pestle and mortar. For DSC analysis approximately 5 mg of samples was used. Samples were held at 30 °C for 5 min and then they were heated up to 300 °C at a 10 K/min rate, where they remained for another 5 min. For the TG analysis approximately 35–55 mg of the sample was used following the same program as the DSC analysis.

2.3.3. Sorption analysis

For Static Vapor Sorption (SVS) tests, materials are dried at 120 °C for 24 h to ensure the anhydrous state is achieved. A Memmert constant climate chamber HPP110eco was employed to uniformly introduce moisture to 10 g of each material. A program was configured to maintain a constant RH (25 %, 50 %, and 75 %) and 25 °C for 24 h, followed by 10 % RH and 25 °C for an additional 24 h. Mass measurements were recorded in-situ throughout the 48-hour program.

2.3.4. Charge and discharge analysis

For discharge analysis a custom-built open reactor was employed, with a continuous flow of humid air directed upward through the fixed bed of materials from the base. A Cellkraft P-50 modular humidity generator is used to produce moist air which is fed into a reactor containing a predetermined volume of material (Fig. 2a). A set of three thermocouples are used to measure temperature uplift and bulk temperature and three load cells at the reactor's base are used to make in-situ mass recordings.

Static charge analysis (SCA) experiments were performed on 4 g of materials, with a broad range of hydration states, using the Ohaus MB120 equipment. The hydrated samples were extracted from the packed bed of the discharge reactor following 2 h of discharge, which contained moisture quantities ranging from 0.4 to 1.8 g. The SCA measurements were conducted at a temperature of 150 °C, and mass recordings were taken until a change of less than 1 mg was observed continuously for 120 s, indicating stabilisation.

As with the discharge reaction, and open reactor design was employed for the dynamic charge analysis (DCA). A Leister Le Mini (Inline air heater) was used in combination with a Brooks MR3000 series flow meter, to create a flow of high-temperature air that passes through a packed bed of each material, with a volume of 400 cm^3 (Fig. 2b). The experiment was monitored using an Ohaus EX10202 scale to measure in-situ mass changes. Additionally, Type K thermocouples were strategically positioned at the inlet, bulk, and outlet locations to measure localised temperature variations. Three charge temperatures (120 °C, 150 °C, 200 °C) and two flow rates (25 & 50 l/min) were selected for the analysis. Before conducting the experiment, the material was hydrated at 25 °C and 25 % relative humidity (RH) until a mass increase corresponding to the hexahydrate was achieved.

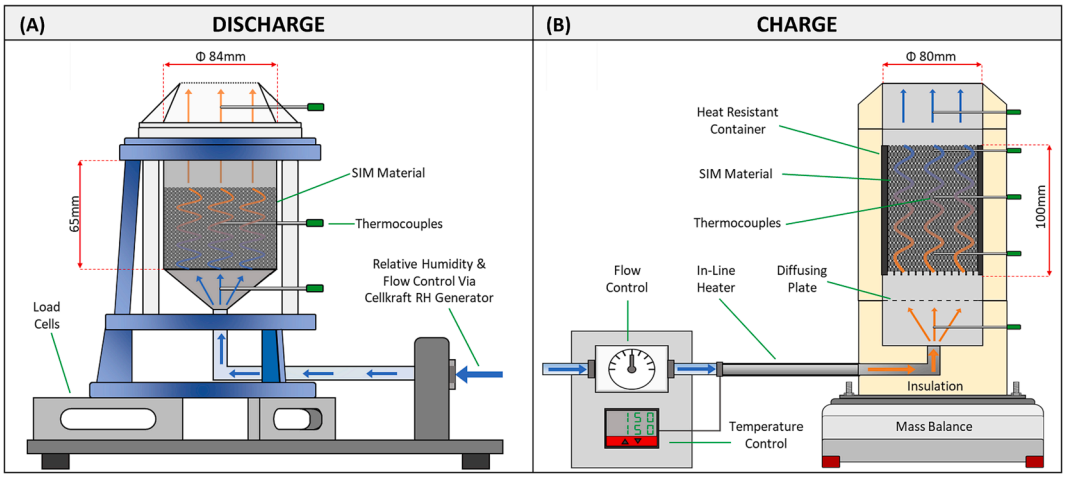

Fig. 2. Experimental apparatus for investigating discharge (A) and charge (B) performance of a typical thermochemical material.

3. Results & discussion

3.1. Physical characterisation

3.1.1. Microscopy

SEM was utilised to examine the internal morphology of the bead composites. Fig. 3 presents the micrographs of the cross-sections for mEG40 and mEG100, representing the two extremes in this study. Micrographs were captured at magnifications 20× and 500× to highlight the presence of salt within the internal matrix. At both magnifications, mEG40 exhibits clear internal porosity, with a limited presence of salt crystals, even at the higher magnification. This suggests that the salt does not form large clusters within the matrix but rather creates a thin layer across the matrix's surface area. Conversely, mEG100 displays less porosity at the lower magnification, evident by a more uniform coverage of solid material and fewer visible pores. At higher magnifications, the formation of salt crystals within the matrix structure is evident, to the extent that the underlying matrix scaffolding is unseen. Although internal porosity is still apparent, the substantial quantity of salt present may overfill these voids upon expansion during hydration.

Fig. 4 shows the EDS maps for the CSA of the composites. Three colours are used to represent different elements: Blue for carbon, Yellow for calcium, and Red for chlorine. Across all samples, there is a good spread of yellow and red regions or a combination of the two, which appears as orange, indicating an even distribution of salt in the pores of the beads. The mEG40 sample shows numerous dark areas, which suggests the presence of numerous pores. The high porosity observed in the mEG40 sample is due to the lower salt concentration, allowing for more void spaces in the material. As the salt concentration in the samples increases, the dark areas, indicative of pores, become less prominent, suggesting a decrease in porosity. This suggests a reduction in porosity as the salt content increases. The mEG100 sample shows minimal black

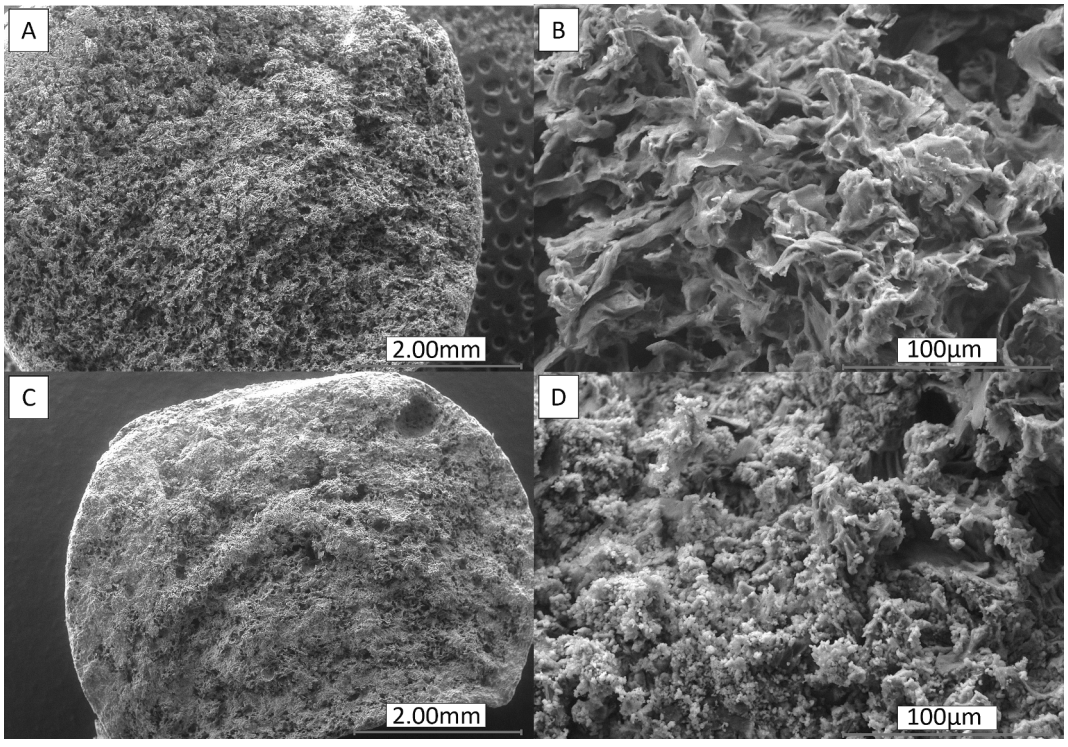

Fig. 3. SEM images of the composite cross-sectional area. mEG40 (A-B) and mEG100 (C-D).

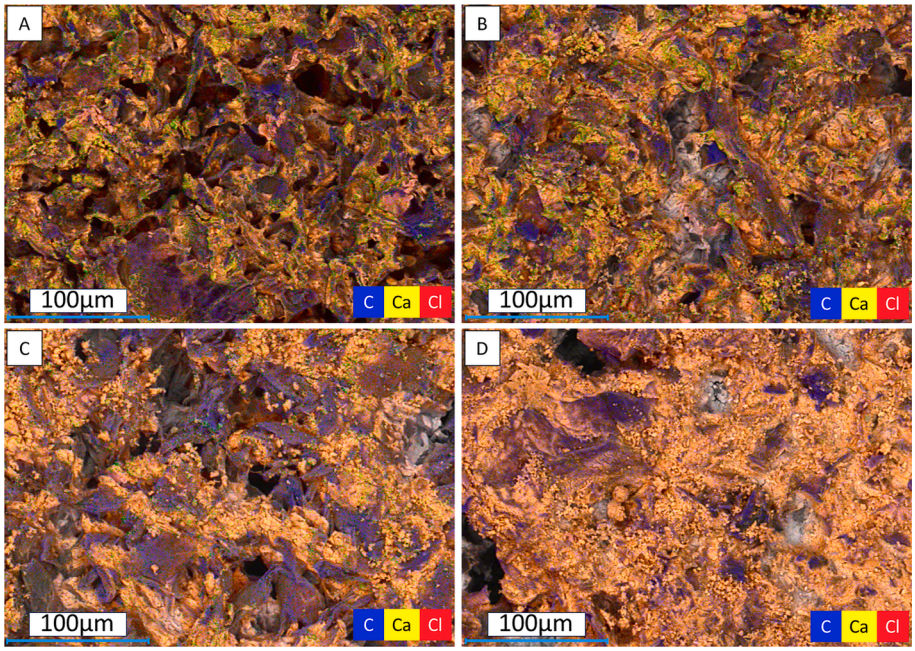

Fig. 4. EDS Maps of the composite cross-sectional area. mEG40 (A), mEG60 (B), mEG80 (C), and mEG100 (D).

areas, visually indicating a lack of porosity resulting from the maximum capacity of salt filling these voids. The dominance of orange colour in the mEG100 sample, representing the presence of $CaCl_2$, indicates that the salt has filled the majority of the available pore space.

3.1.2. Material composition

Table 2 presents the combined physical characteristics and thermal properties of the four bead composites. An increase in salt wt% is observed as the salt concentration in the bath rises. However, this increase in the bead does not follow the linear pattern as observed in the salt bath concentration. The elevation from 40 % to 60 % salt concentration yields a 7.2 % increase in salt wt%, whereas the transition from mEG80 to mEG100 results in only a 1.7 % increase within the bead. This suggests that it is not necessary to utilise fully saturated solutions to achieve salt levels close to maximum capacity.

The size distribution of the beads may explain the reduced levels of salt observed at higher concentrations. The higher salt concentration in the salt bath causes a higher degree of constriction of the beads, leading to a smaller bead diameter at higher concentrations. This could be attributed to the larger osmotic pressure drawing water out of the bead mixture and restricting the pore size before adequate gelation of the beads takes place.

Both the salt wt% and bulk density values are utilised to calculate the salt volumetric density, which plays a crucial role in determining the maximum energy storage capacity of the STES material. The relationship between the salt volumetric density and the porosity of each material reveals that beads produced with the highest salt bath concentration exhibit the highest salt volumetric density but the lowest porosity within the material.

Achieving an optimal STES material requires a balance between maximising both these values. While a larger salt volumetric density increases the theoretical energy storage capacity, it will also reduce porosity to a point of pore blockages. This leads to decreased charge/discharge reactions, due to the limited diffusion of H_2O molecules through the matrix [34]. The extent to which these factors influence kinetics will determine the realistic 'best case' salt volumetric density and the recommended salt bath concentration for synthesis.

Fig. 5 presents the pore size distribution results for four composites with varied salt concentrations. The samples with the lowest salt concentration, namely mEG40 and mEG60, exhibited a nominal pore size ($Ø_{pore}$) of 20.2 µm. In contrast, the composites with higher salt concentrations (mEG80 and mEG100) demonstrated a reduction in nominal

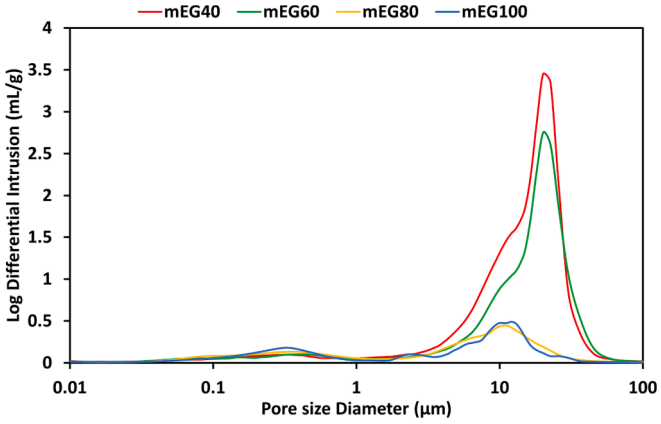

Fig. 5. MIP pore size distributions for the mEG/Alg based composites.

Table 2
Combined physical characteristics and hygrothermal properties of four composites.

Sample	Salt Wt [%]	Bulk Density [g/cm^3]	Size Distribution [mm]	Salt Volumetric Density [g/cm^3]	Porosity [%]	Thermal Conductivity [W/mK]	Specific Heat Capacity [MJ/m^3 K]	Energy Density [kJ/kg]
mEG100	77.2	0.68	5.9	0.52	41.5	0.36	0.53	1281
mEG80	75.0	0.65	5.9	0.49	46.1	0.35	0.53	1230
mEG60	70.9	0.47	6.1	0.33	70.6	0.33	0.31	1163
mEG40	63.7	0.34	6.2	0.22	74.9	0.32	0.29	1052

pore size at 10.7 μm and 12.1 μm respectively.

The mEG40 and mEG60 samples have higher maximum values for the log of intrusion with a larger peak width, indicating a greater overall porosity and a larger pore size range compared to the mEG80 and mEG100 samples. This suggests that the internal pores of the lower salt concentration samples are only coated in salt, while the pores in the higher salt concentration samples have begun to fill. This trend aligns with the observed porosity values, as there was a significant decrease of 24.5 % between the mEG60 and mEG80 samples. This decrease in porosity is undesirable as it reduces the effective surface area for the salt-air interaction essential to reaction kinetics. Furthermore, salt expansion requires adequate space within the matrix to facilitate volume changes, without which there is a risk of promoting leakage. Given the limited decrease in porosity of 4.3 % observed between the mEG60 to mEG40 sample, it is reasonable to deduce that the porosity of an unimpregnated matrix would approximate 80 %. This estimate aligns with the known characteristics of porous activated carbon, which shares similarities with the matrix under investigation [25].

3.2. Thermal characterisation

3.2.1. Thermal transport

The thermal conductivity values for the samples show a small increase as the salt content of the bead is increased. This can be attributed to the salt filling up the pores, which inherently has a higher thermal conductivity than air, thus increasing the value for the composite. However, since the salt itself does not have a high thermal conductivity, this change is minimal. For comparison, pure anhydrous calcium chloride prills have a thermal conductivity of 0.15 W/mK, which is less than half of the values observed for the developed composites under the same conditions. Higher thermal conductivity is generally desirable as it facilitates efficient heat transfer. Therefore, based on this data, it can be inferred that the samples with higher salt content (mEG80 and mEG100) do not exhibit a significant improvement in thermal conductivity compared to the samples with lower salt content (mEG40 and mEG60).

The specific heat capacity values for the samples show a notable increase of 60 % between mEG60 and mEG80. This increase again can be attributed to the salt filling up the pores, which increases the specific heat capacity of that volume fraction. Additionally, the slight decrease in bead diameter may slightly increase the packing density of the material, contributing to the overall increase in specific heat capacity. Higher specific heat capacity indicates that more energy is required to elevate temperatures of the material via sensible heat storage. This characteristic is not desirable for applications that aim to store thermal energy for a longer duration, as the energy stored as sensible heat will be lost during longer storage periods. However, such losses are negligible when compared to the amount of heat chemically stored within the composites.

3.2.2. Energy storage capacity

The energy density results from the DSC analysis are shown in Table 2. These values represent the dehydration enthalpy and the sensible heat of the materials although the latter will be minimal in comparison. The resulting enthalpy values followed the same trend as the salt wt% values, whereby as salt wt% increases, energy density increases. Fig. 6 shows the normalised energy density vs normalised salt wt% with respect to their maximum values. Similar trends are observed between these values, showing that all the hydrated salt contributes to the materials' energy density.

The TGA analysis of the four composites is presented in Fig. 7. The mEG40 sample displays two distinct peaks in the derivative weight curve, with the first peak observed at 130 °C and the second peak at 170 °C. Subsequently, the curve plateaus at 190 °C, with a sample wt% of 59 %. Similarly, the mEG60 sample exhibits two peaks in the derivative weight curve, occurring at 140 °C and 180 °C, respectively. The curve then flattens out at 200 °C, with the wt% reaching 56 %. In

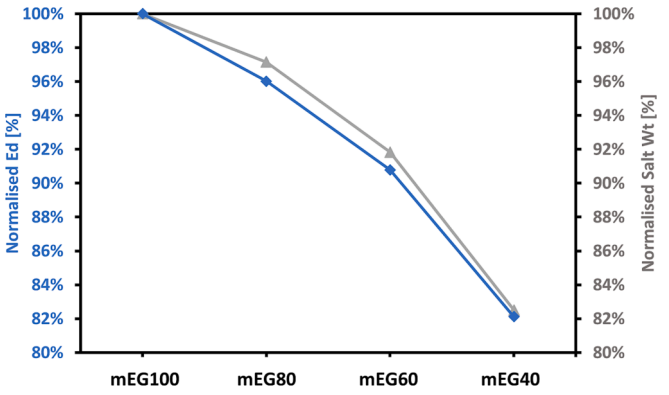

Fig. 6. Normalised data of Energy Density (Blue) and Salt Wt% (Grey) with respect to their maximum value for the saturated sample (mEG100). (For interpretation of the references to colour in this figure legend, the reader is referred to the web version of this article.)

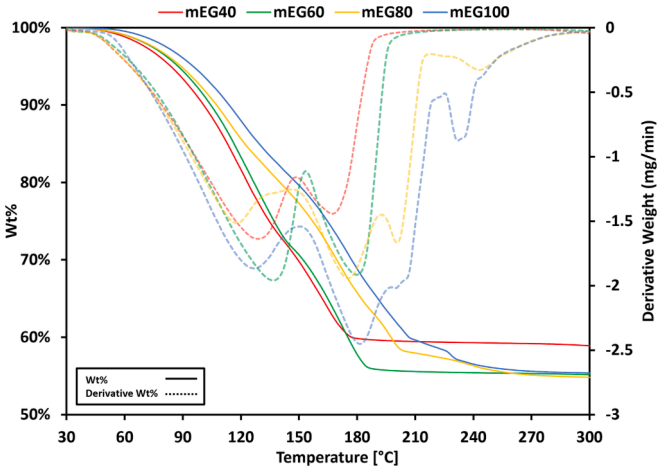

Fig. 7. Thermal gravimetric analysis of the four composites. Wt% change highlighted in bold. Derivative weight change highlighted in dash.

contrast, the mEG80 and mEG100 samples demonstrate more complex behavior, characterised by four peaks in their derivative weight curves. The mEG80 sample shows peaks at 120 °C, 175 °C, 200 °C, and 240 °C, while the mEG100 sample exhibits peaks at 125 °C, 180 °C, 200 °C, and 235 °C.

At the end of the analysis, both mEG80 and mEG100 samples have a wt% of 55 %. The observed lag in the wt% curves as the salt content increases can be attributed to multiple factors. Firstly, the presence of a thicker layer of salt in the mEG60 sample compared to the mEG40 sample contributes to the delayed weight loss. Additionally, with the increase in salt content in the mEG80 and mEG100 samples, the pore size decreases, leading to a mass transfer limitation. This arises as the smaller pores hinder moisture removal, evident from the appearance of multiple peaks in the derivative weight curves.

Table 3 indicates that the H_2O wt% values are marginally higher than expected. This discrepancy may be attributed to the alginate

Table 3
Comparison of Theoretical Hexahydrate-Based Expected H_2O wt% Values with Actual TGA.

	mEG40	mEG60	mEG80	mEG100
Salt wt%	63.7 %	70.9 %	75.0 %	77.2 %
Expected H_2O wt%	39.3 %	41.9 %	43.3 %	44.1 %
Actual H_2O wt%	41.4 %	45.0 %	45.3 %	44.7 %
Addition H_2O wt%	2.1 %	3.1 %	2.0 %	0.6 %

fraction of the composite, which will be more accessible to moisture in samples with lower salt content. Additionally, there is a slight increase in the derivative weight beyond 240 °C, which is likely due to the thermal degradation of the alginate polymer above 200 °C [30]. This effect is more pronounced in the lower salt concentration samples, as they are completely dry well before reaching this temperature onset.

3.3. Water sorption

Fig. 8 shows the moisture absorption curves over 24 h for the SVS tests completed under 25 % RH, 50 % RH, and 75 % RH. Notably, the first condition is below the DRH for $CaCl_2$, while the latter two exceed the DRH. Subsequently, each material underwent a desorption cycle at a low RH of 10 % for an additional 24 h.

Tests were carried out on large samples (10 g) of each composite in their standard composition. This approach was intended to provide a more realistic assessment of moisture uptake compared to the small-scale tests often employed in Dynamic Vapor Sorption (DVS). The absorption curves under all conditions initially demonstrated a maximum rate of moisture uptake, which gradually declined over the course of the 24-hour period.

For tests at 25 % RH, which falls below the DRH, an inverse relationship was observed between the salt wt% and the rate of moisture uptake. The samples with lower salt content, mEG40 and mEG60, appeared to be nearing their maximum moisture uptake after 24 h. In contrast, samples with higher salt content, mEG80 and mEG100, exhibited a linear rate of moisture absorption after approximately 12 h, likely due to reduced internal porosity that restricts moisture penetration to the centre of the material. Table 4 details the wt% gain for each sample after 24 h and the corresponding hydration state equivalent. The data indicates that mEG40 and mEG60 are near their maximum hydration state of $6H_2O$, with values of 5.8 and 5.4 respectively, whereas mEG80 and mEG100 are significantly below this state, with values of 4.7 and 4.0 respectively.

Elevating the humidity to 50 % RH, which is above the DRH, the trend of increasing uptake rates with decreasing salt wt% continues. However, under these conditions, mEG40 has essentially reached its moisture uptake capacity, while the other samples are close to this state. All moisture uptake equivalents for these samples surpass the maximum crystalline hexahydrate state, seemingly converging to the state observed in the mEG40 sample, which is around 10.6 H_2O. This observation highlights the impact of deliquescence on the moisture uptake rate. Deliquescence facilitates an improved transfer of moisture through the material due to the liquid–solid reaction, as opposed to the gas–solid reaction observed below the DRH. This phenomenon accounts for the heightened heat output curves in studies focusing on the discharge reaction above the DRH, as opposed to below it [31].

Table 4
Maximum Wt% Gain values achieved and corresponding hydration state equivalents for each sample at the three conditions completed during SVS.

Sample	Wt% Gain			Hydrate Equivalent ($CaCl_2.XH_2O$)		
	25 % RH	50 % RH	75 % RH	25 % RH	50 % RH	75 % RH
mEG40	60.0 %	109.2 %	144.0 %	5.8	10.6	13.9
mEG60	62.1 %	112.6 %	165.5 %	5.4	9.8	14.4
mEG80	58.0 %	114.8 %	157.2 %	4.7	9.4	12.8
mEG100	50.1 %	120.2 %	186.5 %	4.0	9.6	14.9

At the highest tested condition of 75 % RH, the uptake curves are notably higher than at 50 % RH, suggesting that the degree of deliquescence increases with the level of humidity above the DRH. Contrary to the trends observed at lower humidities, the uptake rate at 75 % RH does not follow a clear pattern: mEG40 < mEG80 < mEG60 < mEG100. The pronounced uptake in mEG100 may be attributed to salt leakage from the material, which would allow for the unhindered absorption of moisture from the air.

From the graph in Fig. 8c, it is evident that the mEG40 sample is nearing its maximum moisture uptake, while mEG100 continues to demonstrate a relatively high rate of uptake after 24 h. The moisture equivalent data (Table 4) reveals that mEG100 has reached 14.9 water equivalents, while mEG40 is at 13.9, indicating that the salt within mEG40 is potentially restricted from further uptake, possibly because it is encapsulated within the matrix. This containment could be advantageous for the cycling stability of the materials, as it may reduce the likelihood of the salt overhydrating, leaking, and forming agglomerates between charge and discharge cycles.

A visual inspection was conducted to provide an understanding of the material conditions during the absorption cycle. A camera rig was set up to capture a timelapse across the 24-hour absorption period, enabling observation of the composites in situ. Fig. 9 presents a series of images during absorption at initial (t = 0 h), mid (t = 12 h), and final (t = 24 h) time intervals for all four composite samples under static conditions of 50 % RH and 25 °C. These images offer a direct visual assessment of the material's behavior that is not readily evident from SVS or DVS data alone.

The images captured at the 24-hour mark provides a clear visual indication of sample stability. For the mEG40 sample, minimal salt leakage is evident, with only small droplets forming from four beads. However, there is a noticeable trend where the incidence of salt leakage escalates with an increase in the salt wt%. This culminates in the

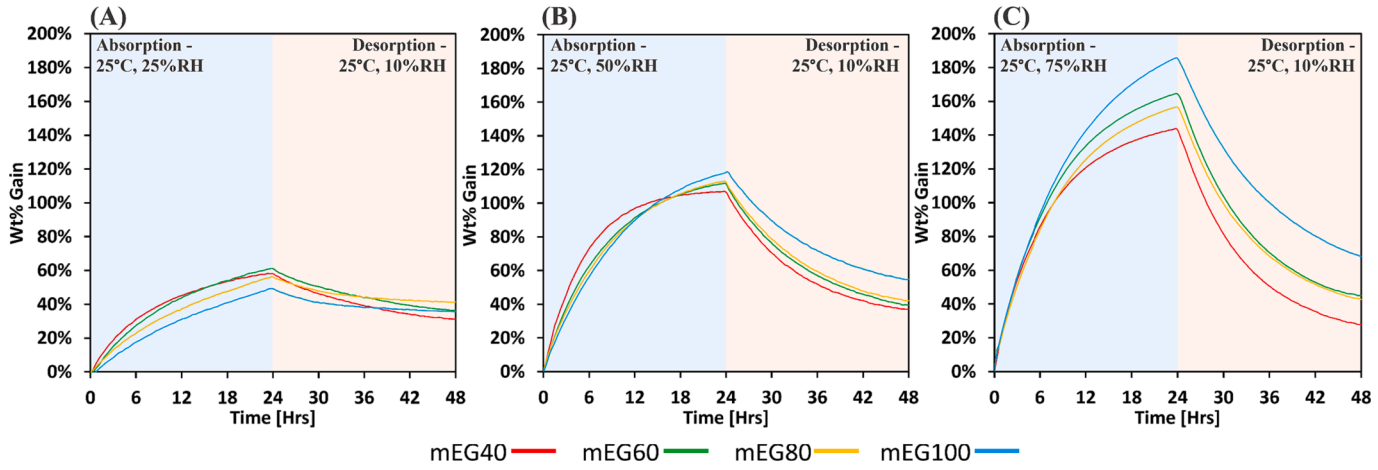

Fig. 8. SVS curves for cycles consisting of 24hr absorption followed by 24hr desorption. Absorption at 25 % RH 25 °C (A). Absorption at 50 % RH 25 °C (B). Absorption at 75 % RH 25 °C (C). All desorption was done under 10 % RH 25 °C.

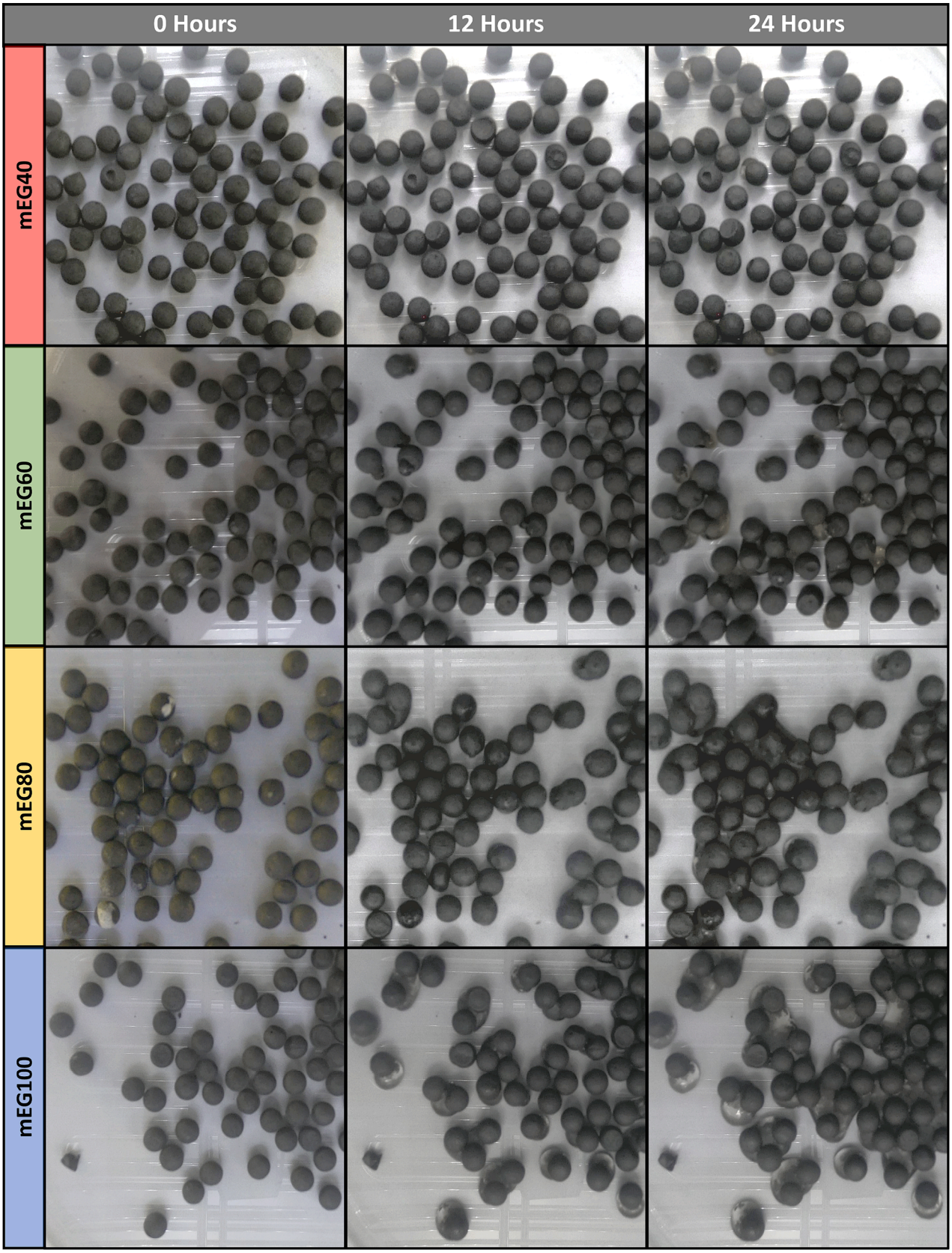

Fig. 9. Static Vapor Sorption at 25 °C/50 % RH after t = 0 hrs, t = 12 hrs, and t = 24 hrs.

mEG100 sample, where the leakage is so extensive that the entire composite appears to be enveloped by a salt solution. This occurs even when the mEG100 is 1 equivalent of water less than the mEG40 sample at the 24 h image.

While a higher salt wt% is generally preferred to maximise energy storage capacity, the visual evidence suggests a trade-off. The apparent detrimental effects, such as the extensive leakage observed, imply that optimising for maximum salt content may inadvertently lead to cyclic and systemic issues, diminishing performance over time.

3.4. Discharge analysis

3.4.1. 2-hour discharge analysis

Fig. 10 and Fig. 11 display the temperature uplift data and mass uplift data, respectively, for the six reactor conditions, varying in RH% (60 %, 70 %, 80 %) and flow rate (20 and 30 l/min), across the four different composites. All composites maintain the characteristic heat uplift profile, characterised by a rapid increase to a peak temperature uplift, followed by a gradual decrease.

The average temperature drop from the peak to the 2-hour mark decreases with increasing salt content in the composites (5.9–1.3 °C for mEG40 – mEG100). This suggests that composites with higher salt concentrations (mEG80 and mEG100) exhibit more stable heat release. However, the average peak temperatures for the composites show a decrease as salt concentrations are increased, showing that the heat release capacity of the composite is influenced by the salt concentration (14.2 – 11.4 °C for mEG60 – mEG100). The higher salt content reduces the kinetics preventing the higher temperatures experienced at the start, however the kinetics appear to stabilise, and a more consistent heat output is seen even after 2 h which can also be contributed to more salt availability. Considering the mEG100 has more than twice the amount of salt per unit volume compared to mEG40, mEG100 is only on average 1.3 °C higher at the 2-hour mark.

The average time to reach peak uplift temperature increases as the salt content increases (12.8–21.3 mins for mEG40 - mEG100). This indicates that composites with higher salt concentrations require more time to reach their maximum heat release capacity. This is attributed to the limited diffusion of moisture into the material to initiate the exothermic reaction. The average moisture uptake rate shows a slight increase as the salt content increases (0.16–0.18 g/min for mEG40 – mEG100). This suggests that composites with higher salt concentrations have a slightly higher capacity to absorb moisture from the air, however this could be because leakage of the salt from the composite due to minimum porosity allowing for more salt to be accessible for further deliquescence. This phenomenon could be contributing to the degradation of composite material experienced by the mEG100 shown in Fig. 12b. This results in the non-cyclic ability of this material and is a main factor in its dismissal in tests going forward. The average total energy over a 2-hour period varies for the different composites: mEG40 (36.8 kJ), mEG60 (39.4 kJ), mEG80 (40.9 kJ), and mEG100 (36.4 kJ). Notably, there is an increase in total energy from mEG40 to mEG80, followed by a slight decrease to mEG100.

Fig. 12c shows the total energy/mass uptake results, effectively showing the efficiency of heat output. Among all the conditions tested, the mEG100 composite exhibits the lowest ratio, indicating a lower energy output compared to the amount of moisture it has absorbed. This could be attributed to a leakage phenomenon that encourages additional deliquescence, thereby reducing the overall energy output. Generally, as the salt content is increased, there is a decreasing trend in the calculated ratio, except for the two middle samples (mEG60 and mEG80) which demonstrate relatively better performance in certain instances. Based on these findings, further longevity tests were conducted on the mEG40 and mEG60 composites.

3.4.2. 8-hour discharge analysis

In assessing the longevity and discharge characteristics of mEG40 and mEG60, tests were conducted under lower RH conditions (40 % RH and 50 % RH). These conditions were selected to limit overhydration beyond the hexahydrate state during the 8-hour test and were informed by the observation in SVS that these materials exhibited good visual stability, with minimal leakage, over a 24-hour period at 50 % RH.

The temperature uplift curves over the 8-hour duration are presented in Fig. 13a. These profiles consistently demonstrate that peak temperature values decrease as humidity input decreases, aligning with previous results for 2-hour tests (3.4.1). Notably, mEG60 outperformed mEG40 under both discharge conditions. It registered both a higher peak temperature and a higher final temperature at the end of the 8-hour test. This superior performance of mEG60 can be attributed to its higher salt

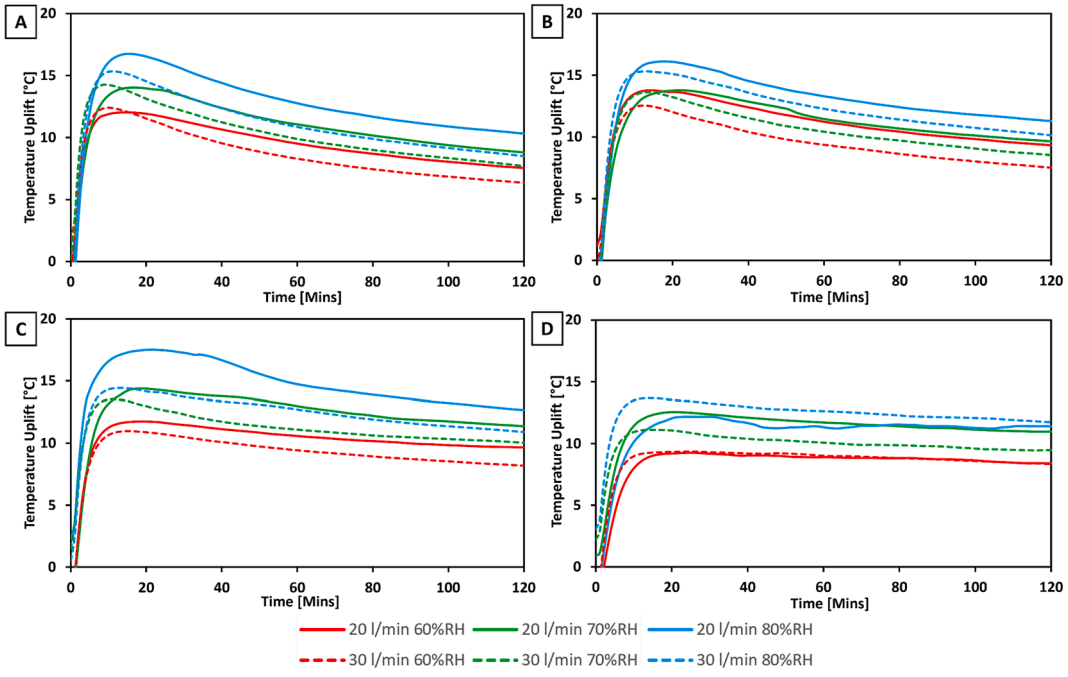

Fig. 10. Temperature uplift curves for 2-hour discharge experiments. mEG40 (A). mEG60 (B). mEG80 (C). mEG100 (D).

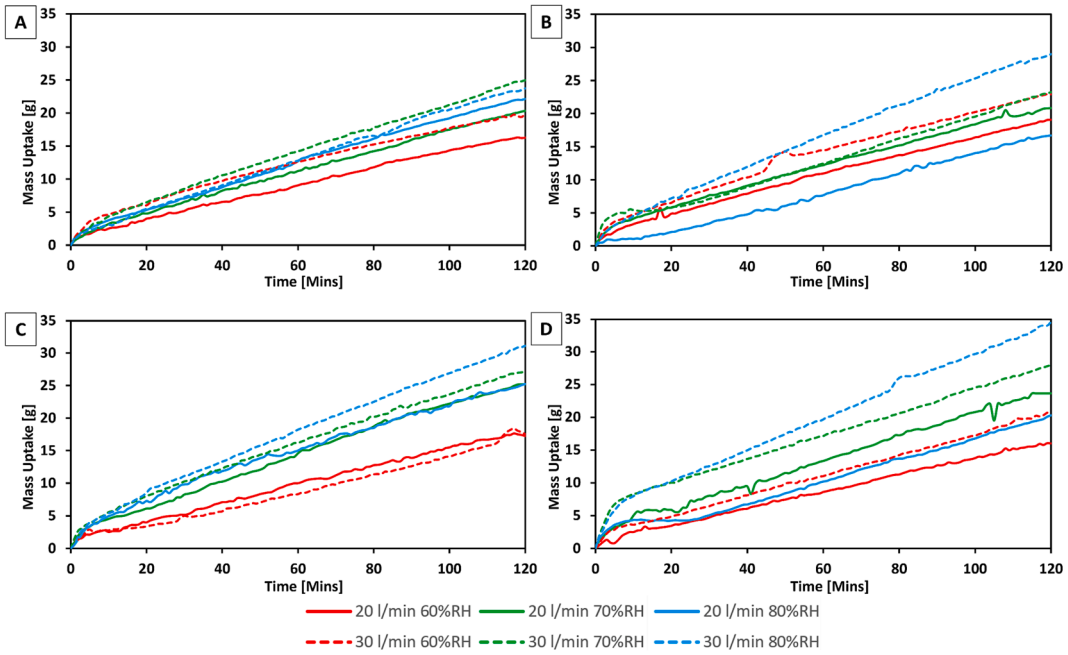

Fig. 11. Mass uptake curves for 2-hour discharge experiments. mEG40 (A). mEG60 (B). mEG80 (C). mEG100 (D).

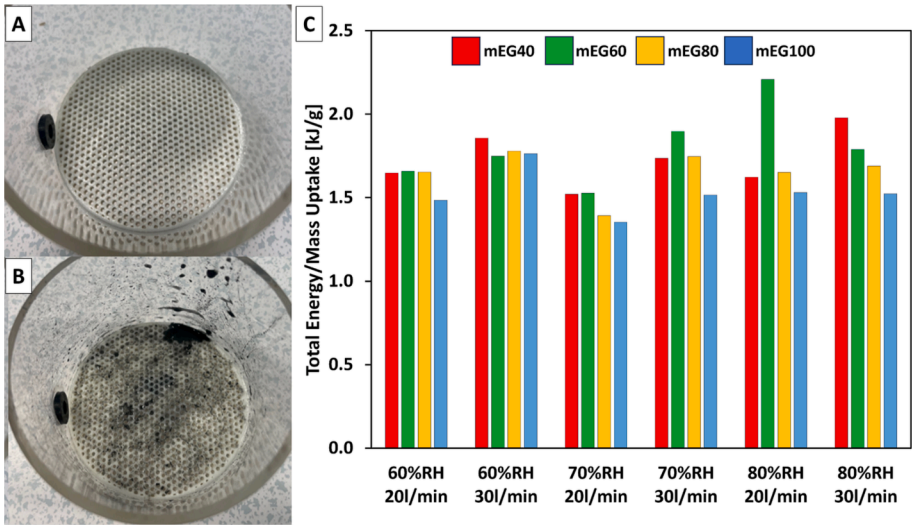

Fig. 12. Discharge RIG container after 2hr cycle for mEG40, mEG60, and mEG80 (A), and mEG100 (B). Total energy/ mass uptake for each condition (C).

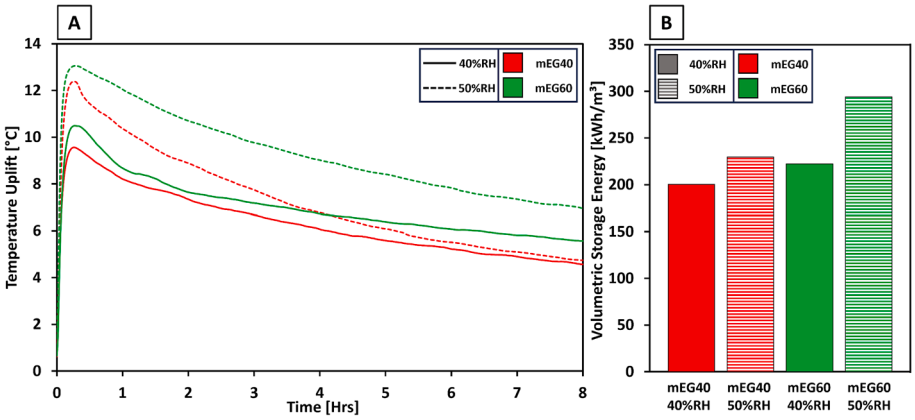

Fig. 13. Temperature uplift curves for 8-hour discharge experiments (A). Total Energy Output over 8 h of discharge (B).

content, which offers more reactive material without compromising reaction kinetics, owing to its porosity that is comparable to that of mEG40. Fig. 13b illustrates the volumetric storage energy for each material under the respective conditions, further confirming the advantage of mEG60. mEG60 achieved a volumetric storage energy of 294 kWh/m^3, surpassing the mEG40, which reached a maximum of 230 kWh/m^3.

Fig. 14a presents the moisture uptake curves for the 8-hour discharge tests. The data shows that the heat energy output corresponds with moisture uptake, similar to the temperature uplift trend. Notably, the moisture uptake rate decreases over time, which accounts for the observed decrease in heat output as the reaction nears completion.

The moisture content at the top and bottom of the reactor is shown in Fig. 14b, specifically after 4 and 8 h of the discharge test. The results align with the mass uptake curves, indicating a greater increase in moisture content during the initial 4 h than in the latter 4 h of the test. It is observed that there is consistently more moisture at the bottom of the reactor than at the top due to the introduction of moisture at the base of the fixed bed, highlighting the importance of reactor design for even hydration over all materials and durations. Over the course of the test, the difference in moisture content between the top and bottom decreases. In the case of the mEG60 at 50 % RH, the moisture content at the top and bottom is nearly the same at the 8-hour mark, suggesting a uniform distribution of moisture throughout the bed.

Fig. 15 depicts the condition of the materials and their average moisture content after an 8-hour period. All four materials demonstrate structural integrity, retaining their spherical form, yet they exhibit differences in surface characteristics. The mEG40 sample, despite having a higher hydration equivalent in both scenarios, appears less wet compared to mEG60. This is attributed to mEG60′s higher salt content and reduced porosity, which results in the salt swelling and deliquescing closer to its maximum capacity. Conversely, the mEG40 sample possesses sufficient pore space to accommodate such expansion without displaying a similar level of surface wetness.

Despite the materials being in a state of hydration beyond the hexahydrate form, a significant temperature uplift (5–7 °C) is still recorded at the 8-hour point for all test cases. Fig. 16 considers two models of moisture absorption. The first model assumes a uniform hydration throughout the bead, as suggested by a single value from moisture analysis. The second model proposes a hydration gradient from the surface to the centre of the bead, with the surface being overhydrated and the centre containing partially reacted salt. This gradient could explain the continued release of heat energy beyond 8 h, despite the average state of hydration across the vertical column suggesting a beyond complete reaction.

3.5. Charge analysis

3.5.1. Static charge analysis (SCA)

Following the six 2-hour discharge experiments for each composite, SCA was conducted on four grams of material sampled from the top and bottom sections of the reactor. With the discharge reactions' time frames and the corresponding mass uptake data, it was evident that the samples exhibited a broad range of moisture equivalents, spanning between $CaCl_2{\cdot}2H_2O$ to $CaCl_2{\cdot}6H_2O$ This allowed for twelve SCA experiments on each composite over a broad range of hydration states.

SCA was performed using an MB120 analyser, programmed to maintain a static temperature of 150 °C. The temperature of the chamber was continuously monitored with a thermocouple positioned directly above the sample, ensuring that any variations due to the endothermic dehydration reaction was accounted for and that a steady temperature was maintained throughout the experiment. Fig. 17 highlights the dehydration curves derived from the SCA of each composite. As the salt content within a composite increased, the rate of the dehydration reaction rapidly decreased. This observation suggests that higher salt concentrations impede moisture removal, resulting in a greater mass transfer resistance during the dehydration of the core. One plausible hypothesis for the observed trend is that the dehydration mechanism initiates at the composite's surface and progresses towards the centre. During this process, the salt within the composite may transition into a liquid state prior to complete dehydration, a transition that begins above 40 °C as indicated by the TGA results (**3.2.1**) and supported by literature [30,35], given the melting point of $CaCl_2{\cdot}6H_2O$ is approximately 29–30 °C [36,37]. This transition allows for salt mobility and recrystallisation, leading to localised crystalline plugs which impede the porous network. As the salt content increases and the dehydration front moves towards the composite's centre, the resulting pore restrictions increasingly impede moisture transport. Consequently, the crystalline or liquid salt mixture becomes more restricted within the composite, significantly slowing down the dehydration kinetics. This phenomenon is well documented in the literature, with the formation of a salt crust on alternative composite options impeding dehydration kinetics [26,38,39].

Table 5 presents the average chemical dehydration times for each material within the moisture levels ranging from 0.6 to 1.4 g. These times have been normalised to establish a comparative scale of

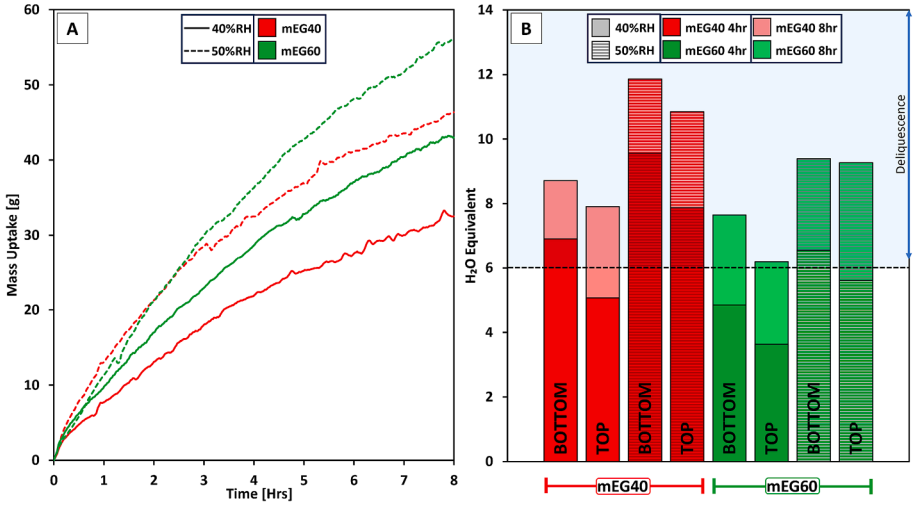

Fig. 14. (A) Moisture uptake curves for 8-hour discharge experiments. (B) Comparison of moisture content, expressed as hydration state equivalent, at the top and bottom of the discharge reactor after 4 h (Front) and 8 h (Back) of operation at a flow rate of 25 l/min, under two different relative humidity conditions: 40 % RH and 50 % RH.

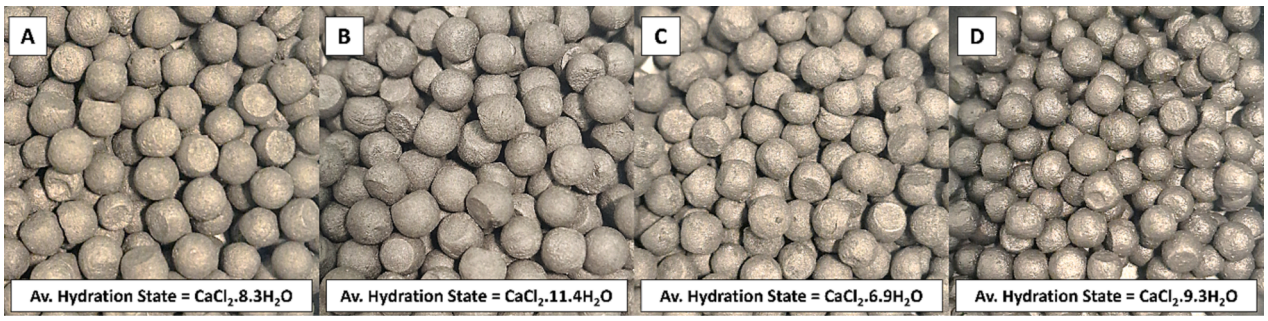

Fig. 15. Optical Images of Beads post 8hr discharge cycles and corresponding average hydration state. mEG40 at 40 % RH (A). mEG40 at 50 % RH (B). mEG60 at 40 % RH (C). mEG60 at 50 % RH (D).

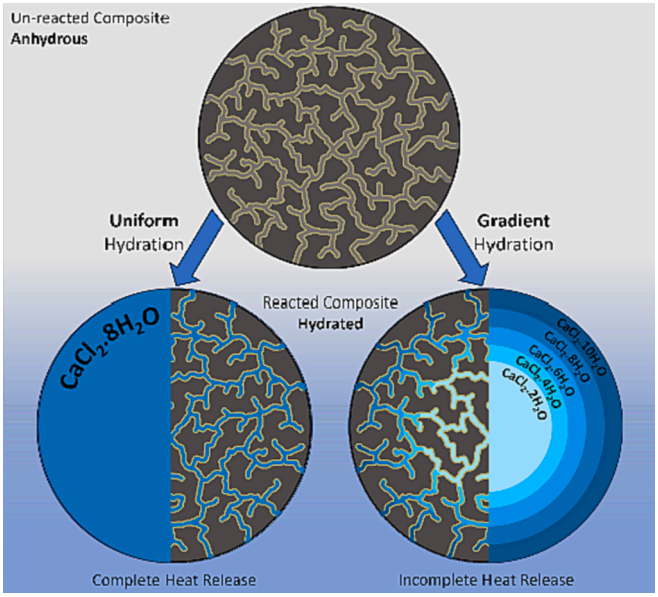

Fig. 16. Two considerations for the localised state of discharge after 8hrs.

dehydration efficiency, by dividing the minimum dehydration time (mEG40) by the dehydration time of the sample under consideration. Under consistent static heating conditions, the data reveals that as salt wt% decreases the dehydration efficiency of the composite significantly increases, with mEG40 drying at more than four times the rate of mEG100, as indicated by mEG100′s normalised drying efficiency of 0.23. Consequently, although mEG40 would require a larger volume of material and possibly multiple vessel exchanges during the heat capture phase, the enhanced dehydration efficiency could potentially outweigh these logistical considerations.

Nonetheless, it is imperative to consider the equilibrium between the kinetics of heat capture and the storage density of the material. Despite the appeal of lower salt concentrations which may yield even higher dehydration efficiency, such as those found in a hypothetical mEG20 sample, the subsequent decrease in storage density is unfavorable. Such evaluations are essential in determining the optimal material composition for effective heat energy capture and storage.

3.5.2. *Dynamic charge analysis (DCA)*

The desorption performance of the composites was evaluated within a dynamic environment at a larger scale (400 cm^3), utilising a fixed bed reactor with air flow through the materials. These tests were conducted under three temperatures (90, 120, and 150 °C) and two flow rates (25 and 50 l/min). The resulting desorption profiles for the composites across these six conditions are displayed in Fig. 18.

In general, the manual termination of tests was prompted by the equilibrium between output and inlet temperatures, indicative of zero heat absorption. Notably, the tests conducted at 90 °C frequently extended overnight due to the extended reaction timescales, often culminating in outlet temperature stabilisation prior to the intended conclusion of the test. Despite this, the mass loss at 90 °C did not show the same level of stabilisation, suggesting a substantial deceleration in the rate of moisture desorption towards the end of the period at this temperature. Given this observation, a threshold of 95 % desorption was adopted further on for comparison purposes. Independently of the

Table 5
Static Dehydration Data for moisture levels between 0.6 and 1.4 g.

Sample	Average Dehydration Time [Mins]	Normalised Dehydration Efficiency
mEG40	23.5	1.00
mEG60	43.5	0.54
mEG80	62.1	0.38
mEG100	103.1	0.23

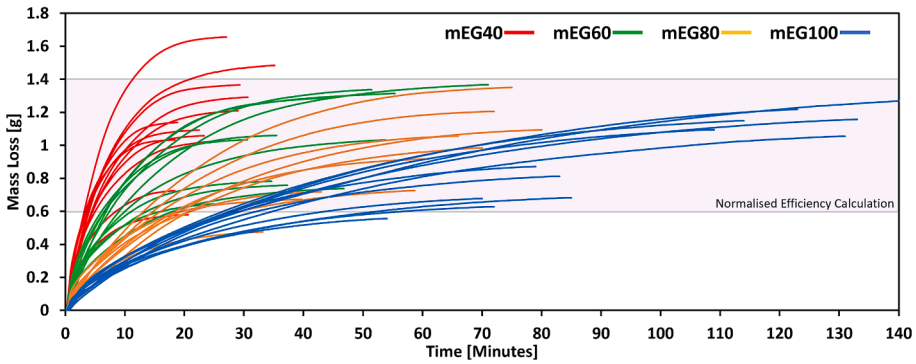

Fig. 17. Static dehydration curves of 4 g of material containing between 0.4 and 1.8 g of moisture.

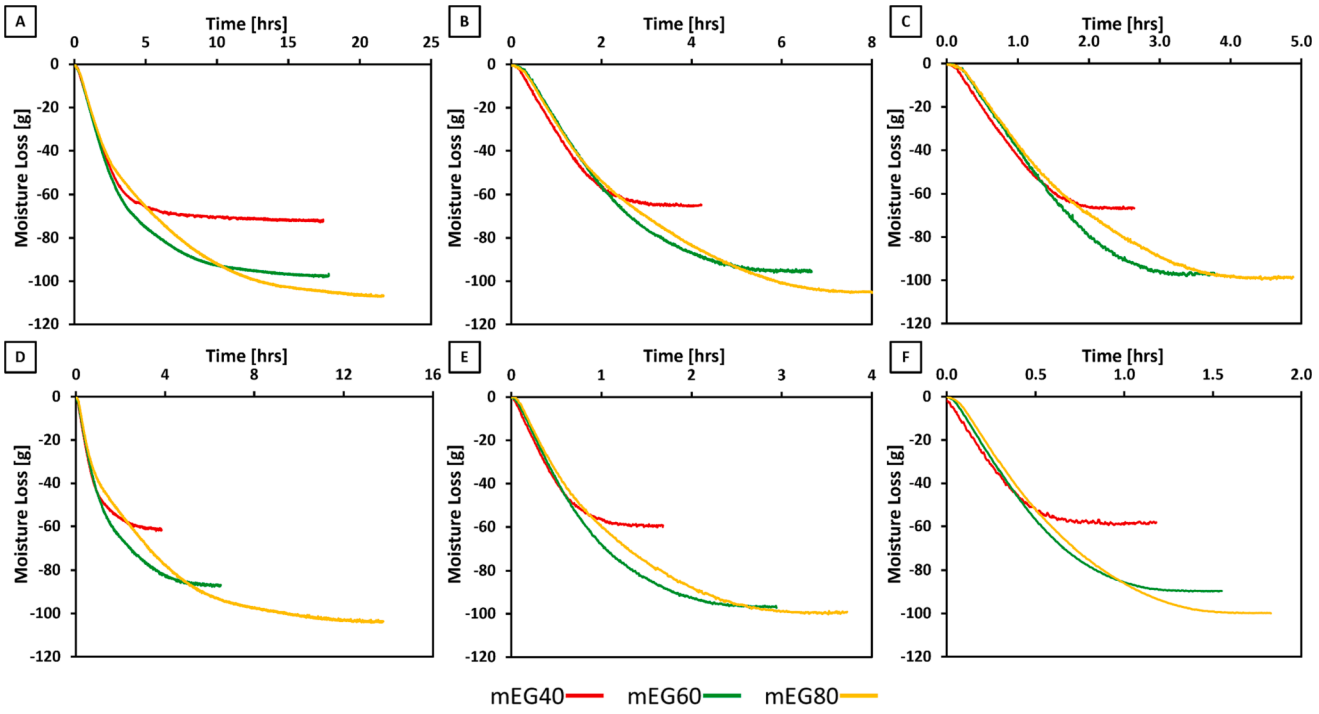

Fig. 18. Raw mass loss curves for composites. 6 conditions considered: 25 l/min 90 °C (A), 25 l/min 120 °C (B), 25 l/min 150 °C (C), 50 l/min 90 °C (D), 50 l/min 90 °C (E), 50 l/min 150 °C (F).

specific conditions, each material demonstrated an initial phase of constant mass loss rate, which transitioned to a decelerating rate of mass loss until the reaction's end.

Variation among the samples regarding the duration of constant mass loss rate is observed. On average, mEG40 maintained a linear mass loss rate for 73 % of the total mass lost. In contrast, mEG60 and mEG80 displayed a shortened duration of constant mass loss rate, accounting for 63 % and 44 % of the total mass lost, respectively. These differences reflect the availability of accessible salt within the composites. mEG80 possesses the least accessible salt, likely due to internal areas being restricted by larger salt quantities located near the surface.

Fig. 19 shows the input heat energy required to achieve percentage values of the maximum moisture desorbed to understand the trends in charge efficiency between reaction conditions. The supplied heat energy (E) between t = 0 and t at a percentage of the total mass loss is calculated using equation (2). Here m(t) is the mass of the air at each 10-second interval, C_p is the specific heat capacity of air, ΔT(t) is the temperature change between reactor inlet and room temperature (RT = 20 °C) at each 10-second interval. Owing to the observed discrepancies in total mass loss within identical samples, which stems from the challenges associated with attaining a perfectly hexahydrate state in the RH climate chamber, the energy values have been normalised relative to their theoretical hexahydrate wt% values.

$$E = \sum_{t=0}^{t_{\%Charged}} \boldsymbol{m}(t) \cdot \boldsymbol{C_p} \cdot \Delta \boldsymbol{T}(t) \tag{2}$$

A distinct trend emerges in evaluating the charge energy across all three composites. As the flow temperature rises, the efficiency of charge, indicated by a reduction in required heat energy, increases. This trend holds at both tested flow rates, with a notable decrease in the amount of heat energy supplied when the temperature is raised from 90 °C to 120 °C. Beyond this point, the efficiency gains from increasing the temperature to 150 °C are less pronounced, suggesting a diminishing return on efficiency as temperature rises, with expectations that a further increase to 180 °C would yield similar efficiency to 150 °C.

The impact of flow rate on charge efficiency is less clear when analysing the data from a 95 wt% loss point of view. Nevertheless, a more detailed examination of the wt% loss at individual rates, as depicted in

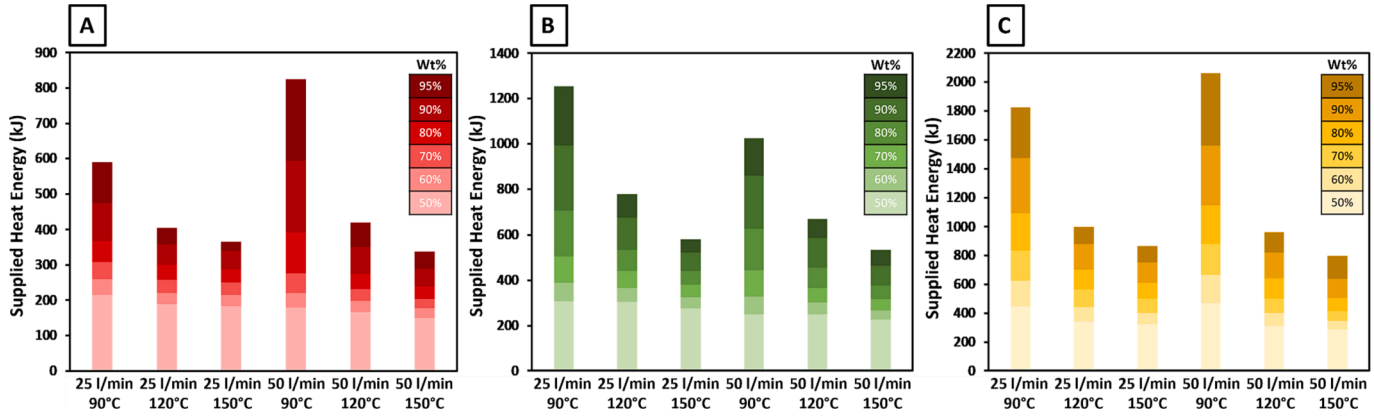

Fig. 19. Graded supplied heat energy for up to 95 % moisture desorption for mEG40 (A), mEG60 (B), mEG80 (C).

Fig. 20, indicates that at desorption levels ranging from 50 to 70 wt%, a higher flow rate tends to lower the energy required. When comparing the energy demands across the three composites, several patterns are observed. It is consistently seen that as the salt content within the composites increases, so does the energy necessary to achieve a given level of wt% loss. Noticeably for mEG80, the efficiency is considerably less at 90 °C compared to mEG40 and mEG60. However, this efficiency deficit is greatly reduced when the temperature is increased to 120 °C, suggesting that higher temperatures make mEG80 more competitive in terms of energy demand for desorption.

For a fair comparison of the composites' charging efficiency, a metric of energy input per unit of moisture desorbed (kJ/g) was devised. Fig. 21 highlights this relationship, presenting the values for each composite and charge condition at both 50 %wt and 95 %wt desorption stages. It is evident from Fig. 20 that there is an established trend in the energy required to reach the hexahydrate state, with mEG40 requiring the least and mEG80 the most. However, considering the variance in moisture content to be desorbed across composites, which follows the same trend, the presented data in Fig. 21 allows for a better comparison of charge energy efficiency on a per gram basis.

From the analysis, it is apparent that the energy per gram necessary for 95 wt% desorption is markedly higher compared to that for 50 wt%, reflecting the non-linear mass loss characteristic of the latter stages of the charging process. When comparing the composites directly, while the trend of increasing energy per gram with increasing salt content is consistent, the mEG60 composite demonstrates competitive energy efficiency. At the 50 wt% stage, it performs comparably to, and occasionally better than, mEG40, particularly in the 90 °C charge experiments, where both composites average 5.6 kJ/g under the tested conditions. However, at 95 wt% charge completion, mEG40 shows improved efficiency over mEG60, with respective energy requirements of 7.9 and 9.0 kJ/g. These results suggests that mEG60 could potentially be the composite of choice, despite its generally higher energy per gram requirement. The definitive choice would depend on specific operational constraints, whether the limitation is space, or a certain energy density needed for the system's viability.

4. Conclusion

Successful control of salt loading ($CaCl_2$) within an expanded graphite and alginate matrix was achieved, maintaining the composite's morphology with minimal physical changes. While maximising salt loading within the composite may seem advantageous for enhancing heat storage capacity, the drawbacks identified in this study indicate a preference for a lower salt bath concentration, and subsequent lower salt loading.

Across the considered saturation concentrations ranging from 40 % to 100 %, the salt wt% within the matrix varied from 63.7 to 77.2 %, corresponding to energy density between 1052 and 1281 kJ/kg respectively. These findings emphasise the marginal advantages of targeting maximum capacity.

There is a notable decrease in porosity between mEG60 and mEG80 which suggests a shift in salt distribution, transitioning from thin layers coating the pore surfaces to the salt beginning to fill the pores. This is visually evident from the observed internal structures.

The discharge analysis revealed that composites with higher salt content, particularly the mEG100, displayed reduced energy efficiency and even sustained structural degradation over a 2-hour period. In the 8-hour discharge tests, both mEG40 and mEG60 composites maintained structural integrity. mEG60 achieved the highest energy output of 294 kWh/m^3, outperforming mEG40's maximum of 230 kWh/m^3.

The efficiency of charge in both static and dynamic discharge scenarios for the composites indicates that lower salt content correlates with greater efficiency. While static tests show clear differences in efficiency based on salt content, these disparities become less pronounced in a dynamic environment. In such dynamic conditions, all materials exhibit an initial constant rate of mass loss, with this linear phase extending longer in composites with lower salt content. Among the variables tested, a temperature increase has a more pronounced effect on enhancing charge efficiency than flow rate adjustments. While mEG40 has the lowest average charge energy demand to achieve 95 wt% dehydration (7.9 kJ/g), the mEG60 shows competitive performance (9.0 kJ/g) and could be the preferred choice depending on specific operational constraints.

This work highlights the importance of controlled salt content, particularly for deliquescing salt hydrates. Nonetheless, it is essential to recognise that not all salt hydrates will experience deliquescence under the conditions tested, suggesting that pursuing maximum salt loading remains a valid strategy. Further enhancements in the kinetics of the materials might be achieved by considering other factors, such as composite size, to ensure optimal charging and discharging kinetics.

CRediT authorship contribution statement

Jack Reynolds: Writing – review & editing, Writing – original draft, Visualization, Methodology, Investigation, Formal analysis, Data curation, Conceptualization. **Bahaa Abbas:** Writing – review & editing, Investigation, Data curation. **Geraint Sullivan:** Writing – review & editing, Investigation, Data curation. **Jonathon Elvins:** Writing – review & editing, Supervision, Resources, Project administration, Funding acquisition, Conceptualization. **Eifion Jewell:** Writing – review & editing, Supervision, Resources, Project administration, Funding acquisition, Conceptualization. **Justin Searle:** Writing – review & editing, Supervision, Resources. **Lorena Skevi:** Writing – review &

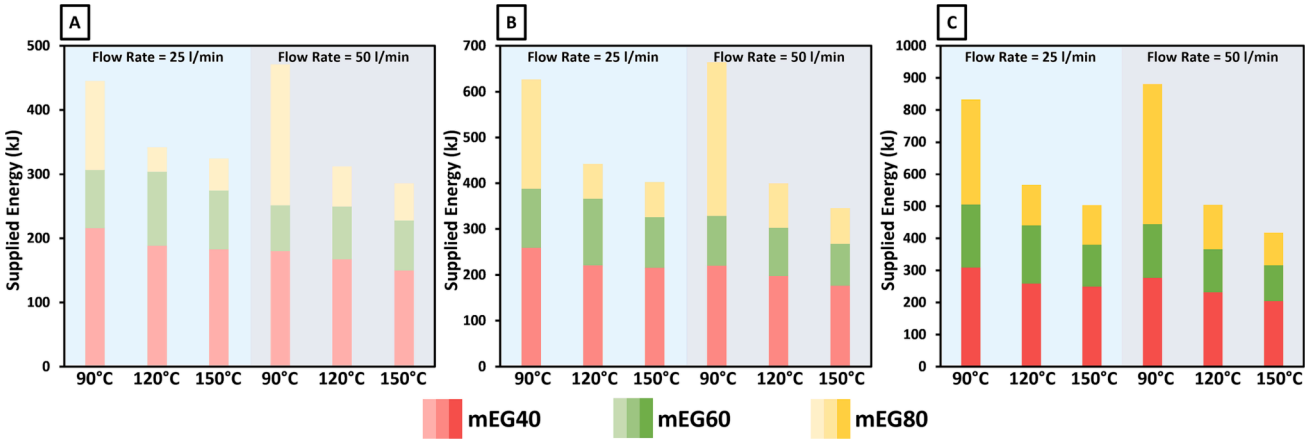

Fig. 20. Overlayed supplied heat energy for the three considered composites to achieve moisture losses of 50 wt% (A), 60 wt% (B), 70 wt% (C).

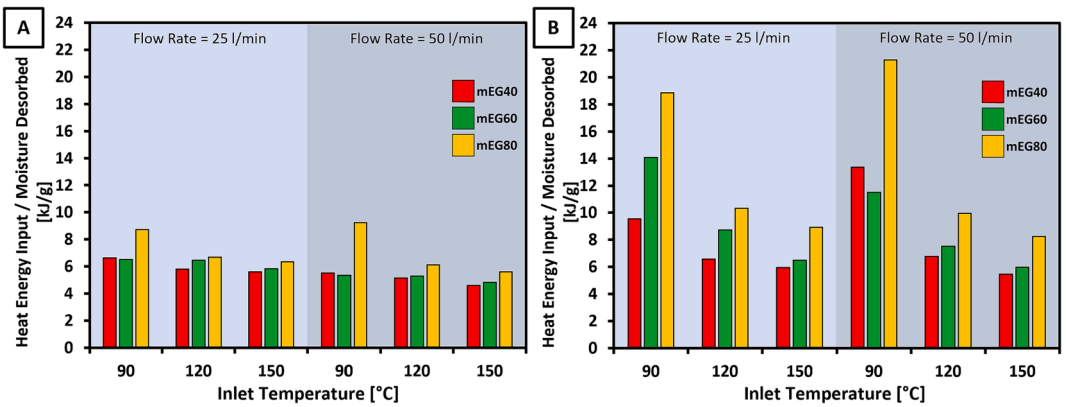

Fig. 21. Heat energy Input divided by the average moisture desorbed for each sample under the 6 conditions. 50 % moisture desorbed (A). 95 % moisture desorbed (B).

editing, Investigation, Formal analysis, Data curation. **Xinyuan Ke:** Writing – review & editing, Investigation, Data curation.

Declaration of competing interest

The authors declare that they have no known competing financial interests or personal relationships that could have appeared to influence the work reported in this paper.

Data availability

No data was used for the research described in the article.

Acknowledgements

The authors would like to thank the Materials and Manufacturing Academy and COATED CDT (COATED M2A) in Swansea University, TATA Steel Colors, Engineering and Physical Sciences Research Council (EPSRC via UKRI) EP/S02252X/1, and the European Social Fund via the Welsh Government (WEFO) (c80816) for supporting the work described in this article.

References

[1] Ofgem, Ofgem's Future Insights Series: The Decarbonisation of Heat; 2016. https://www.ofgem.gov.uk/system/files/docs/2016/11/ofgem_future_insights_programme_-_the_decarbonisation_of_heat.pdf [accessed 1 Oct 2023].
[2] Mitchell R, Natarajan S. UK Passivhaus and the energy performance gap. Energy Build 2020;224:110240. https://doi.org/10.1016/j.enbuild.2020.110240.
[3] Rotaheat's Technology. https://rotaheat.co.uk/technology/. [accessed 1 Oct 2023].
[4] N'Tsoukpoe KE, Liu H, Le Pierrès N, Luo L. A review on long-term sorption solar energy storage. Renew Sustain Energy Rev 2009;13:2385–96. https://doi.org/10.1016/j.rser.2009.05.008.
[5] Thekdi A, Nimbalkar SU. Industrial Waste Heat Recovery : Potential Applications, Available Technologies and Crosscutting R&D Opportunities. Oak Ridge Natl Lab 82; 2015. https://doi.org/10.2172/1185778.
[6] Woolley E, Luo Y, Simeone A. Industrial waste heat recovery: A systematic approach. Sustain Energy Technol Assess 2018;29:50–9. https://doi.org/10.1016/j.seta.2018.07.001.
[7] Jarimi H, Aydin D, Yanan Z, et al. Review on the recent progress of thermochemical materials and processes for solar thermal energy storage and industrial waste heat recovery. Int J Low-Carbon Technol 2019;14:44–69.
[8] Ndiaye K, Ginestet S, Cyr M. Thermal energy storage based on cementitious materials: A review. AIMS Energy 2018;6:97–120. https://doi.org/10.3934/energy.2018.1.97.
[9] Aydin D, Casey SP, Riffat S. The latest advancements on thermochemical heat storage systems. Renew Sustain Energy Rev 2015;41:356–67. https://doi.org/10.1016/j.rser.2014.08.054.
[10] Mohapatra D, Nandanavanam J. Salt in matrix for thermochemical energy storage - A review. Mater Today Proc 2022. https://doi.org/10.1016/j.matpr.2022.05.453.
[11] Donkers PAJ, Sögütoglu LC, Huinink HP, et al. A review of salt hydrates for seasonal heat storage in domestic applications. Appl Energy 2017;199:45–68. https://doi.org/10.1016/j.apenergy.2017.04.080.
[12] Gaeini M, Rouws AL, Salari JWO, et al. Characterization of microencapsulated and impregnated porous host materials based on calcium chloride for thermochemical energy storage. Appl Energy 2018. https://doi.org/10.1016/j.apenergy.2017.12.131.
[13] Aristov YI. New family of solid sorbents for adsorptive cooling: Material scientist approach. J Eng Thermophys 2007;16:63–72. https://doi.org/10.1134/S1810232807020026.
[14] Tatsidjodoung P, Le N, Heintz J, et al. Experimental and numerical investigations of a zeolite 13X / water reactor for solar heat storage in buildings. Energy Convers Manag 2016;108:488–500. https://doi.org/10.1016/j.enconman.2015.11.011.
[15] Mahon D, Claudio G, Eames PC. An experimental investigation to assess the potential of using MgSO4 impregnation and Mg2+ ion exchange to enhance the performance of 13X molecular sieves for interseasonal domestic thermochemical energy storage. Energy Convers Manag 2017;150:870–7. https://doi.org/10.1016/j.enconman.2017.03.080.
[16] Wei S, Han R, Su Y, et al. Development of pomegranate-type CaCl 2 @ C composites via a scalable one- pot pyrolysis strategy for solar-driven thermochemical heat storage. Energy Convers Manag 2020;212:112694. https://doi.org/10.1016/j.enconman.2020.112694.
[17] Posern K, Osburg A. Determination of the heat storage performance of thermochemical heat storage materials based on SrCl2 and MgSO4. J Therm Anal Calorim 2018. https://doi.org/10.1007/s10973-017-6861-8.
[18] Courbon E, D'Ans P, Permyakova A, et al. A new composite sorbent based on SrBr 2 and silica gel for solar energy storage application with high energy storage density and stability. Appl Energy 2017;190:1184–94. https://doi.org/10.1016/j.apenergy.2017.01.041.
[19] Zhang YN, Wang RZ, Zhao YJ, et al. Development and thermochemical characterizations of vermiculite/SrBr 2 composite sorbents for low-temperature heat storage. Energy 2016;115:120–8. https://doi.org/10.1016/j.energy.2016.08.108.
[20] Sutton RJ, Jewell E, Elvins J, et al. Characterising the discharge cycle of CaCl2 and LiNO3 hydrated salts within a vermiculite composite scaffold for thermochemical storage. Energy Build 2018;162:109–20. https://doi.org/10.1016/j.enbuild.2017.11.068.
[21] Chen Z, Zhang Y, Zhang Y, et al. A study on vermiculite-based salt mixture composite materials for low-grade thermochemical adsorption heat storage. Energy 2023;278:127986. https://doi.org/10.1016/j.energy.2023.127986.
[22] Aydin D, Casey SP, Chen X, Riffat S. Novel " open-sorption pipe " reactor for solar thermal energy storage. Energy Convers Manag 2016;121:321–34. https://doi.org/10.1016/j.enconman.2016.05.045.
[23] Casey SP, Aydin D, Elvins J, Riffat S. Salt impregnated desiccant matrices for 'open' thermochemical energy conversion and storage – Improving energy density utilisation through hygrodynamic & thermodynamic reactor design. Energy Convers Manag 2017;142:426–40. https://doi.org/10.1016/j.enconman.2017.03.066.
[24] Gordeeva LG, Aristov YI. Composites "salt inside porous matrix" for adsorption heat transformation: A current state-of-the-art and new trends. Int J Low-Carbon Technol 2012;7:288–302. https://doi.org/10.1093/ijlct/cts050.
[25] Casey SP, Elvins J, Riffat S, Robinson A. Salt impregnated desiccant matrices for "open" thermochemical energy storage - Selection, synthesis and characterisation of candidate materials. Energy Build 2014;84:412–25. https://doi.org/10.1016/j.enbuild.2014.08.028.
[26] Cammarata A, Verda V, Sciacovelli A, Ding Y. Hybrid strontium bromide-natural graphite composites for low to medium temperature thermochemical energy storage: Formulation, fabrication and performance investigation. Energy Convers Manag 2018;166:233–40. https://doi.org/10.1016/j.enconman.2018.04.031.
[27] Salviati S, Carosio F, Saracco G, Fina A. Hydrated salt/graphite/polyelectrolyte organic-inorganic hybrids for efficient thermochemical storage. Nanomaterials 2019;9:420. https://doi.org/10.3390/nano9030420.
[28] Salviati S, Carosio F, Cantamessa F, et al. Ice-templated nanocellulose porous structure enhances thermochemical storage kinetics in hydrated salt/graphite

composites. Renew Energy 2020;160:698–706. https://doi.org/10.1016/j.renene.2020.07.036.
[29] Aarts J, van Ravensteijn B, Fischer H, et al. Polymeric stabilization of salt hydrates for thermochemical energy storage. Appl Energy 2023;341:121068. https://doi.org/10.1016/j.apenergy.2023.121068.
[30] Kallenberger PA, Posern K, Linnow K, et al. Alginate-Derived salt/polymer composites for thermochemical heat storage. Adv Sustain Syst 2018;2:1700160. https://doi.org/10.1002/adsu.201700160.
[31] Heitmann S, Osburg A. Alterations of a CaCl 2 Alginate Composite for Thermochemical Heat Storage during the Hydration in a 1 L Packed Bed Laboratory Reactor; 2023, p. 593–604. https://doi.org/10.3390/thermo3040035.
[32] Reynolds J, Williams R, Elvins J, et al. Development and characterisation of an alginate and expanded graphite based composite for thermochemical heat storage. J Mater Sci 2023. https://doi.org/10.1007/s10853-023-08370-1.
[33] Michel B, Mazet N, Mauran S, et al. Thermochemical process for seasonal storage of solar energy: Characterization and modeling of a high density reactive bed. Energy 2012;47:553–63. https://doi.org/10.1016/j.energy.2012.09.029.
[34] Jabbari-Hichri A, Bennici S, Auroux A. CaCl2-containing composites as thermochemical heat storage materials. Sol Energy Mater Sol Cells 2017;172:177–85. https://doi.org/10.1016/j.solmat.2017.07.037.
[35] Rammelberg HU, Osterland T, Priehs B, et al. Thermochemical heat storage materials – Performance of mixed salt hydrates. Sol Energy 2016;136:571–89. https://doi.org/10.1016/j.solener.2016.07.016.
[36] Kenisarin M, Mahkamov K. Salt hydrates as latent heat storage materials: Thermophysical properties and costs. Sol Energy Mater Sol Cells 2016;145:255–86. https://doi.org/10.1016/j.solmat.2015.10.029.
[37] Carlsson B, Stymne H, Wettermark G. An incongruent heat-of-fusion system-CaCl2·6H2O-Made congruent through modification of the chemical composition of the system. Sol Energy 1979;23:343–50. https://doi.org/10.1016/0038-092X(79)90129-4.
[38] Clark R, Mehrabadi A, Farid M. State of the art on salt hydrate thermochemical energy storage systems for use in building applications. J Energy Storage 2020;27:101145. https://doi.org/10.1016/j.est.2019.101145.
[39] Jabbari-Hichri A, Is A, Bennici S, Auroux A. CaCl2-containing composites as thermochemical heat storage materials. Sol Energy Mater Sol Cells 2017. https://doi.org/10.1016/j.solmat.2017.07.037.